

## On The Very Bright Dropouts Selected Using the James Webb Space Telescope NIRCam Instrument

BANGZHENG SUN <sup>1</sup> AND HAOJING YAN <sup>1</sup>

<sup>1</sup>*Department of Physics and Astronomy, University of Missouri - Columbia  
701 S College Avenue  
Columbia, MO 65201, USA*

### ABSTRACT

The selection of candidate high-redshift galaxies using the dropout technique targeting the Lyman-break signature sometimes results in very bright objects, which would be too luminous to be easily explained if they are indeed at the expected redshifts. Here we present a systematic study of very bright dropouts selected through successive bands of the NIRCam instrument onboard the James Webb Space Telescope (JWST). Using the public NIRCam data in four blank fields over 500 arcmin<sup>2</sup>, 300 such objects were found. They have magnitudes in F356W < 25.1 mag or < 26.0 mag depending on the dropout passband, and the vast majority of them (> 80%) have very red F115W–F356W colors > 2.0 mag, which make them qualify as “extremely red objects” (EROs). We focus on the 137 objects that also have mid-IR observations from the JWST MIRI instrument. The analysis of their spectral energy distributions shows that these very bright dropouts are dominated by low-redshift ( $z \sim 1\text{--}4$ ) galaxies ( $\gtrsim 67\%$ ). However, a non-negligible fraction ( $\gtrsim 7\%$ ) could be at high redshifts. Seven of our objects have secure spectroscopic redshifts from the JWST NIRSpec identifications, and the results confirm this picture: while six are low-redshift galaxies at  $z \approx 3$ , one is a known galaxy at  $z = 8.679$  recovered in our sample. If more objects from our sample are confirmed to be at high redshifts, they could pose a severe challenge in explaining their properties, such as the extremely high star formation rates and stellar masses.

### 1. INTRODUCTION

Various kinds of “extremely red objects” (EROs) have been selected over the past three decades by using different color indices involving different infrared (IR) bands as the technologies evolve. The early discoveries were mostly made by comparing the ground-based observations in  $K$ -band ( $\sim 2.2 \mu\text{m}$ ) and in an optical band (e.g., Elston et al. 1988; Hu & Ridgway 1994; Thompson et al. 1999; Scodreggio & Silva 2000), although occasionally deep data in the less red F160W band ( $\sim 1.6 \mu\text{m}$ ) of the Hubble Space Telescope (HST) Near Infrared Camera and Multi-Object Spectrometer (NICMOS) were also used (e.g., Yan et al. 2000). The general interpretation of such EROs is that they are predominantly early-type galaxies at  $z \approx 1$  and that their red IR-to-optical colors are due to their old stellar populations. After the launch of the Spitzer Space Telescope, the ERO selection proceeded to using the Infrared Array Camera (IRAC) 3.6 and/or 4.5  $\mu\text{m}$  channels in IR and the HST Advanced Camera for Surveys (ACS) bands in optical (e.g. Yan et al. 2004). Such EROs are also mostly evolved galaxies but are at higher redshifts of  $z \approx 2\text{--}4$ . The extension in the IR wavelengths by IRAC also allowed the ERO selection through IR colors such as  $K_s - 4.5\mu\text{m}$  involving ground-based  $K_s$  band (e.g., Wang et al. 2012) and F160W  $- 4.5\mu\text{m}$  involving the reddest band (F160W) of the HST Wide Field Camera 3 (WFC3) (e.g., Caputi et al. 2014; Wang et al. 2016; Alcalde Pampilega et al. 2019). The latter ones are also referred to as the “HST-dark” objects because they are extremely weak or even invisible in the deep images taken in any HST bands. Inter-

estingly, the EROs selected using IR color indices consist of not only early-type galaxies dominated by passively evolving stellar populations but also extremely dust-reddened galaxies with strong ongoing star formation embedded by dust (e.g., Wang et al. 2019). In fact, dusty starbursts invisible at  $\lambda < 2 \mu\text{m}$  were already known to exist, for instance the historical submillimeter galaxy (SMG) HDF 850.1 (Cowie et al. 2009; Walter et al. 2012). Many similar SMGs were later revealed (e.g., Zhou et al. 2020; Gómez-Guijarro et al. 2022; Xiao et al. 2023), making them a distinct population among EROs at  $z > 4$  awaiting further exploration.

In a broad sense, the selection of high-redshift (high- $z$ ) galaxies also relies on identifying red colors, which are due to the Lyman-break signature in their spectral energy distributions (SEDs). This is caused by the discrete neutral hydrogen clouds along the sightline that absorb the photons bluer than the Lyman-limit (rest frame  $\lambda < 912\text{\AA}$ ) and those coincide with the Ly $\alpha$  line wavelength (rest frame  $\lambda = 1216\text{\AA}$ ). These absorptions create a sharp discontinuity (“Lyman break”) in the spectrum of a high-redshift (high- $z$ ) galaxy, resulting in a red color index in two adjacent bands that straddle the Lyman break. For this reason, a high- $z$  galaxy would appear to “drop out” from the band to the blue side of the break and “re-appear” in the red band, and this is the basis of the classic “dropout” selection of galaxies at  $z \gtrsim 3$  (Steidel & Hamilton 1992, 1993; Steidel et al. 1995). At  $z > 5$ , the cumulative Ly $\alpha$  line absorptions (“Ly $\alpha$  forest”) are so strong that Lyman break occurs at the rest frame 1216 $\text{\AA}$ . In practice, candidate high- $z$  galaxies selected based on the Lyman-break signature

always have contaminants from red galaxies at low redshifts (“low- $z$  interlopers”), and the most extreme ones could be the aforementioned EROs.

JWST offers unprecedented sensitivity and spatial resolution in the IR wavelengths. It has pushed the redshift record of galaxies to  $z = 14.32$  (Carniani et al. 2024), and thousands of candidates have been selected at  $z \gtrsim 7$  using its NIRCam instrument. In the meantime, it has also brought the study of EROs to a new level (e.g., Rodighiero et al. 2023; Nelson et al. 2023; Gómez-Guijarro et al. 2023; Barrufet et al. 2023; Gibson et al. 2024). When the hunt of high- $z$  galaxies moves forward to higher and higher redshifts, the selected candidates bare more and more similarity to EROs. As an example, galaxies at  $z \gtrsim 12$  should be invisible at  $\lambda < 1.5 \mu\text{m}$ , which could be regarded as being HST-dark.

On the face value, all known EROs are IR-bright. For instance, typical HST-dark galaxies have AB magnitudes of  $\leq 24$  mag at 3–5  $\mu\text{m}$ . Therefore, one might think that the IR brightness could be used to distinguish the two populations. However, EROs being IR-bright reflects more the limitation of the technology at the time when they were first studied than their intrinsic properties. In this context, it is important to study how these two populations overlap in the new JWST era, starting from the bright end. In this work, we aim at the very bright high- $z$  candidates selected using the NIRCam data following the classic dropout technique and investigate how they could be affected by low- $z$  EROs. In order to make our analysis robust, we focus on the fields where the mid-IR imaging data from the JWST MIRI instrument are also available.

The structure of our paper is as follows. We describe the relevant NIRCam and MIRI data in Section 2 and the photometry in Section 3, respectively. The selection of bright dropouts in the NIRCam bands is detailed in Section 4, followed by the analysis of their SEDs in Section 5. Based on their photometric redshifts ( $z_{\text{ph}}$ ), these bright dropouts are broadly categorized in Section 6 as being potential high- $z$  galaxies and possible low- $z$  EROs. A small fraction of our objects have spectroscopic confirmations, which we show in Section 7. We discuss our results in Section 8 and conclude with a summary in Section 9. All magnitudes quoted in this work are in the AB system. All coordinates are in the ICRS frame and Equinox 2000. We adopt a flat  $\Lambda$ CDM cosmology with  $H_0 = 71 \text{ km s}^{-1} \text{ Mpc}^{-1}$ ,  $\Omega_m = 0.27$ , and  $\Omega_\Lambda = 0.73$ .

## 2. JWST NIRCAM AND MIRI IMAGING DATA

We utilize four JWST fields that have both NIRCam and MIRI data, which are summarized in Table 1. These are from the Public Release IMAGING for Extragalactic Research (PRIMER) program (Dunlop et al. 2021) in the COSMOS and the UDS fields, the Cosmic Evolution Early Release Science Survey (CEERS; Finkelstein et al. 2023) in the EGS field, and the JWST Advanced Deep Extragalactic Survey (JADES; Eisenstein et al. 2023a) in the GOODS-S region. These data and their reduction are briefly described below.

### 2.1. Data Description

- **PRIMER in COSMOS and UDS:** two shallow but wide fields. The total areas covered by NIRCam are 137.13 and 185.83 arcmin<sup>2</sup>, respectively, and those covered by MIRI are 100.58 and 112.51 arcmin<sup>2</sup>, respectively. The PRIMER program executed the MIRI observations as the primary and the NIRCam ones as the coordinated parallel while maximizing the overlapping areas between the two. In the end, the overlapping areas between the NIRCam and MIRI observations are 67.80 and 76.91 arcmin<sup>2</sup> for these two fields, respectively. The NIRCam observations utilized eight passbands: F090W, F115W, F150W, and F200W in the short-wavelength channel (SW), and F277W, F356W, F410M, and F444W in the long-wavelength channel (LW). The MIRI observations were in F770W and F1800W. In these two fields, we selected dropouts in F090W, F115W, F150W, F200W, and F277W. To assist the F090W dropout selection, we integrated the HST ACS data from the CANDELS survey (Grogin et al. 2011; Koekemoer et al. 2011) in both COSMOS and UDS.

- **CEERS in EGS:** another shallow but wide field. It was observed in seven NIRCam bands: F115W, F150W, and F200W in the SW channel, and F277W, F356W, F410M, and F444W in the LW channel. The NIRCam coverage is 86.45 arcmin<sup>2</sup>. The MIRI observations were made in smaller areas and were in seven bands: F560W, F770W, F1000W, F1280W, F1500W, F1800W, and F2100W. However, the MIRI footprints are non-overlapping for all these bands, and different parts of the field are covered only by certain sets of filters: (1) F560W and F770W (7.69 arcmin<sup>2</sup> overlapping with NIRCam), (2) F1000W, F1280W, F1500W, and F1800W (3.72 arcmin<sup>2</sup> overlapping with NIRCam), (3) F1500W only (5.15 arcmin<sup>2</sup> overlapping with NIRCam), and (4) F2100W only (no overlap with NIRCam). Due to the lack of the F090W data, we only searched for the F115W, F150W, F200W, and F277W dropouts. We utilized the ancillary HST ACS data from the CANDELS survey to assist the F115W dropout selection.

- **GOODS-S:** the main part of the data are from the JWST Advanced Deep Extragalactic Survey (JADES; Eisenstein et al. 2023a), which made the NIRCam observations in two areas within the GOODS-S field at two different depths, “deep” and “medium” (hereafter JADES-deep and JADES-medium). The data were taken in 9 NIRCam bands: F090W, F115W, F150W, and F200W in the SW channel, and F277W, F335M, F356W, F410M, and F444W in the LW channel. These data are all much deeper than PRIMER and CEERS. We also integrated the NIRCam data from the Pure Parallel Wide Area Legacy Imaging Survey (PANORAMIC, PID 2514; Williams et al. 2024) and those from PID 3215 (Eisenstein et al. 2023b) into the JADES-medium field. The final NIRCam images cover 25.50 and 37.94 arcmin<sup>2</sup> in JADES-deep and JADES-medium, respectively. For MIRI, we combined all the public observations overlapping the JADES coverage into one mosaic per band, which include those from PID 1207 (Rieke et al. 2017), 1283 (Norgaard-Nielsen & Perez-Gonzalez 2017), and 1180 (PI Eisenstein).

Field	R.A. (deg)	Decl. (deg)	Instrument	Pipeline	Context	Area (arcmin <sup>2</sup> )	Exposure (ks)
COSMOS	150.12299	2.34764	NIRCam	1.10.2	1089	137.13	~2.5
			MIRI	1.12.5	1183	100.58	~1.7
			Overlap Area				67.80
UDS	34.35004	-5.20001	NIRCam	1.10.2/1.11.3	1089/1106	185.83	~1.4
			MIRI	1.12.5	1180	112.51	~1.7
			Overlap Area				76.91
CEERS	215.00545	52.93451	NIRCam	1.9.4	1046	86.45	~2.5
			MIRI	1.12.5	1183	~ 5 - 16	~1-8
			Overlap Area				3.72-7.69
JADES (deep)	53.16444	-27.78256	NIRCam	1.12.5	1180	25.50	~14-60
JADES (medium)	53.07011	-27.90011	NIRCam	1.12.4	1140	37.94	~1.5-40
GOODS-S	53.14027	-27.82140	MIRI	1.13.4	1188	32.90	~0.6-142
Overlap Area						20.83/15.99	

**Table 1.** Summary of the fields used in this work, which have data from both NIRCam and MIRI. The nominal exposure times in these fields are given under “Exposure”. The equatorial coordinates are at the field centers, and the sizes of the overlapped regions between the NIRCam and the MIRI coverages are indicated in the “Overlap Area” rows. The version of the JWST data reduction pipeline that we used and the relevant context file (“pmap”) are listed under “Pipeline” and “Context”, respectively. The astrometry that we adopted in the COSMOS, UDS and CEERS fields is that from the HST CANDELS survey, while that in the JADES fields are based on the GAIA DR3.

Eight MIRI bands were utilized by these programs: F560W, F770W, F1000W, F1280W, F1500W, F1800W, F2100W, and F2550W, and the final MIRI images cover 32.90 arcmin<sup>2</sup> in all eight bands. The overlapping areas between NIRCam and MIRI are 20.83 and 15.99 arcmin<sup>2</sup> in JADES-deep and JADES-medium, respectively.

## 2.2. Data Reduction

We reduced all the data in this study on our own using the JWST pipeline (Bushouse et al. 2024). The NIRCam data reduction followed the procedures outlined in Yan et al. (2023b) and Yan et al. (2024). For MIRI, we ran through the similar procedures but with four changes: (1) in the `calwebb_detector1` step, we set `jump.find_showers` to “True” to remove the large residuals on single MIRI exposures due to strong cosmic ray events; (2) for the products after the stage 2 pipeline process, we followed the recipe by Yang et al. (2023) to remove the stripe-like noise pattern in horizontal and/or vertical directions; (3) we then removed the remaining noise patterns by constructing templates on a per-observation and per-filter basis and subtracted the corresponding template from each single exposure; and (4) we excluded the coronagraph areas in each individual exposure by masking their pixels to `DO_NOT_USE` in the data quality array.

## 3. PHOTOMETRY

All the final NIRCam and MIRI mosaics have a pixel scale of 0′′.06, which translates to the AB magnitude zero-point of 26.581. We used `SExtractor` (Bertin & Arnouts 1996) for source extraction and photometry. We treated the NIRCam and the MIRI images separately because the latter have much larger point spread functions (PSFs).

### 3.1. NIRCam photometry for dropout selection

The dropout selection involves the NIRCam data but not the MIRI data. For each field, we ran `SExtractor` in the dual-image mode and adopted F356W-based match-aperture photometry. We chose the F356W band as the detection band for the following reasons: (1) the F356W images are usually the deepest across all bands; (2) the PSF in this band

is sufficiently large, which ensures that the apertures properly determined in this band include all source fluxes in any bluer bands; (3) the F356W images present a notably cleaner background than those in the SW bands.

The source extraction was done by applying a  $5 \times 5$  Gaussian convolution filter with a full width at half maximum (FWHM) of 2 pixels. From the weight images produced by the JWST data reduction pipeline, we derived the “root mean square” (rms) maps using the `astroRMS` routine<sup>1</sup>, which calculates the auto-correlation of the science image pixels due to the drizzling process that should be applied to scale the weight images. These rms maps were used for both the source detection and the estimate of photometric errors. The detection and analysis thresholds were set to 1.0 in `SExtractor`. We adopted the `MAG_ISO` magnitudes and only retained the sources with signal-to-noise ratio (S/N) of at least 5 and `ISOAREA` of at least 10 pixels in the F356W image.

### 3.2. Photometry for spectral energy distributions

When constructing SEDs, a common practice is to use photometry on PSF-matched images, i.e., the images in different bands are all convolved to have the same PSF size as in the band that has the largest PSF. Our SED analysis would involve both the NIRCam and the MIRI data, and PSF-matched photometry across all bands would not be appropriate in this case: smearing the NIRCam data (PSF FWHM 0′′.030 to 0′′.145 from F090W to F444W) to the coarsest MIRI resolution (F2550W PSF FWHM of  $\sim 0′′.803$ ) would blend many unrelated neighbors in the NIRCam images and corrupt the NIRCam photometry.

As the best compromise, we took a hybrid approach. In the NIRCam wavelengths, we prepared another set of NIRCam photometry done on the PSF-matched NIRCam images. For each field, we convolved the images in the bluer bands to the PSF size of the F444W image. The PSFs were derived using isolated stars in the field, following the proce-

<sup>1</sup> See <https://github.com/mmechtley/astroRMS>; we modified the routine slightly by adopting a better source masking functionality.



ture in Ling & Yan (2022). `SExtractor` was again run in the dual-image mode, and this time the F444W image was used as the basis. We again adopted the `MAG_ISO` magnitudes to calculate the colors. A common practice would be to scale up the `MAG_ISO`-based SED to the “total flux” SED by adding the difference between the `MAG_ISO` and the `MAG_AUTO` magnitude in F444W band. As we will show in Section 4, however, a large fraction of our objects have neighbors that would contaminate the `MAG_AUTO` magnitude. Therefore, we chose not to apply such a correction. For isolated, bright ( $m_{444} < 26.5$  mag) sources, we found that the differences between the `MAG_ISO` and the `MAG_AUTO` magnitudes were under 0.05 mag, and the impact of omitting such a correction would only be marginal to the SED analysis.

The MIRI PSF size vary greatly in different bands, which makes the PSF-matched photometry also inappropriate among the MIRI images. Therefore, we ran `SExtractor` in the single-image mode for each MIRI band and adopted the `MAG_ISO` magnitudes. Similar to what was mentioned above for the NIRC*am* images, we also found that the difference between the `MAG_ISO` and the `MAG_AUTO` magnitudes were under 0.05 mag for bright, isolated sources in the MIRI images.

Lastly, we note that we treated any photometry with  $S/N < 2$  as non-detection and adopted the  $2\sigma$  upper limit. Such limits were measured on the rms maps at the source locations using circular apertures of sizes equivalent to those of the `MAG_ISO` apertures.

For simplicity, hereafter we denote the magnitudes in the HST/ACS F435W, F606W, F775W, F814W, and F850LP bands as  $m_{435}$ ,  $m_{606}$ ,  $m_{775}$ ,  $m_{814}$ ,  $m_{850}$ , respectively, those in the JWST/NIRC*am* F090W, F115W, F150W, F200W, F277W, F335M, F356W, F410M, and F444W bands as  $m_{090}$ ,  $m_{115}$ ,  $m_{150}$ ,  $m_{200}$ ,  $m_{277}$ ,  $m_{335}$ ,  $m_{356}$ ,  $m_{410}$ , and  $m_{444}$ , respectively, and those in the JWST/MIRI F560W, F770W, F1000W, F1280W, F1500W, F1800W, F2100W, and F2550W as  $m_{560}$ ,  $m_{770}$ ,  $m_{1000}$ ,  $m_{1280}$ ,  $m_{1500}$ ,  $m_{1800}$ ,  $m_{2100}$ , and  $m_{2550}$ , respectively.

#### 4. SELECTION OF VERY BRIGHT DROPOUTS

As mentioned in Section 3.1, the dropout selection was done using the NIRC*am* photometry based on the non-PSF-matched images. This approach has multiple advantages over using the PSF-matched images, such as no artificially introduced blending problem, less chance of misidentifying a broadened artifact as a source, more accurate  $S/N$  assessment, etc. The potential caveat of biased color indices using non-PSF-matched images has only a marginal impact here for two reasons. First, our objects would be dropouts from the bands bluer than F356W (the vast majority being dropouts from the SW bands), and the `MAG_ISO` aperture defined in F356W is large enough to include most (if not all) of the light in these bands in the first place. Second, the break amplitude is determined by the magnitudes in two adjacent bands whose PSF sizes are close, and the small difference in the fraction of light enclosed by the adopted aperture would only smear the redshift selection function negligibly.

Similar to Yan et al. (2023a,b), we adopted the dropout selection criteria as follows.

(1)  $S/N \geq 5$  in the shift-in band. The shift-in band is the redder band adjacent to the drop-out band. This criterion is to ensure the detection in the shift-in band and the robustness of the measured dropout amplitude.

(2) Dropout amplitude  $\geq 0.8$  mag. The dropout amplitude is the color index between the drop-out and the shift-in bands. As mentioned above, when a source has  $S/N < 2$  in the drop-out band, its magnitude is substituted with the  $2\sigma$  upper limit. This amplitude is chosen because the Lyman-break signature shifted halfway out of the dropout band would create a color index of  $\sim 0.75$  mag between the dropout and shift-in bands for a flat spectrum in  $f_\nu$ .

(3)  $S/N \geq 5$  in at least one more band redder than the shift-in band. All the retained sources have  $S/N \geq 5$  in F356W and the shift-in band, and this additional requirement further ensures the reliability of the detections.

(4)  $S/N < 2$  in all bands bluer than the drop-out band. A legitimate candidate should not be detected in these “veto” bands. This is the most important criterion that distinguishes the dropout selection and the ERO selection, whereas the latter does not have such a requirement.

The candidates thus selected were then visually examined in all bands to ensure that they are real sources and are indeed invisible in the veto bands. In this work, we only study very bright F090W and F115W dropouts with  $m_{356} \leq 25.1$  mag and F150W, F200W, and F277W dropouts with  $m_{356} \leq 26.0$  mag. The objects fainter than these limits are considered “normal” and are discussed in Yan et al. (2023b) (for the F150W, F200W and F277W dropouts) and in Sun & Yan (in preparation, for the F090W and F115W dropouts), respectively. In total, we have found 300 bright dropouts, 137 of which are covered by at least one MIRI band. We focus on these 137 dropouts that have MIRI photometry (with detections or upper limits), which form our main sample and will be discussed next. The other 163 objects form the supplement sample; for the sake of completeness, these objects are listed in Table A.1. In the main sample, there are 59 dropouts in F090W, 36 in F115W, 37 in F150W, 5 in F200W, and none in F277W. Figure 1 shows the image stamps of two objects in each group as examples. If the dropout effect is due to the Lyman break, the nominal redshift ranges of the dropouts in F090W, F115W, F150W, and F200W are  $z \approx 6.4\text{--}8.4$ ,  $8.4\text{--}11.3$ ,  $11.3\text{--}15.4$ ,  $15.4\text{--}21.8$ , respectively. The aforementioned brightness criteria roughly correspond to  $M \approx -22$  mag in rest frame U and B band, respectively.

Interestingly, most of these objects either are very compact or have disk-like morphology. Out of the 300 bright dropouts,  $\sim 48\%$  are compact sources,  $\sim 38\%$  are disk-like,  $\sim 2\%$  are elliptical, and  $\sim 12\%$  are irregular in shape. In the pre-JWST era, one would put the disk-like objects to low redshifts because common wisdom has been that disk galaxies cannot be formed so early in time. However, the JWST observations over the past two years have found a large number of candidate stellar disks at  $z > 2$  and up to  $z \approx 8$  (e.g., Fu-

damoto et al. 2022; Ferreira et al. 2022, 2023; Nelson et al. 2023; Jacobs et al. 2023; Robertson et al. 2023; Kuhn et al. 2024; Yan et al. 2024), which suggest an early formation of stellar disks. Therefore, we chose not to make judgment based on morphology, and all objects were analyzed in the same way.

To demonstrate how the bright dropouts are qualified as EROs, Figure 2 shows the  $m_{115} - m_{356}$  color distribution as a function of  $m_{356}$  for the 137 objects in our main sample, using different symbols for the dropouts from different bands. Even when adopting a very red color of  $m_{115} - m_{356} > 2.0$  mag as the fiducial criterion for EROs, the vast majority (81%) of our bright dropouts would be selected.

## 5. SED ANALYSIS

To better understand the nature of these bright dropouts, we analyzed the SEDs of the objects in the main sample. The SEDs were constructed using the photometry in both NIRCcam and MIRI as detailed in Section 3.2, which was tailored for this purpose. Following the usual practice, we added 0.05 mag in quadrature to the reported photometric errors to account for the possible systematics, e.g., the offsets between the NIRCcam and the MIRI photometry due to the different adopted methods.

### 5.1. Methods and procedures

We fitted the SEDs using three different tools, namely, Le Phare (version 2.2; Arnouts et al. 1999; Ilbert et al. 2006), EAZY (eazy-py version 0.6.4; Brammer et al. 2008), and CIGALE (version 2022.1; Boquien et al. 2019). A major goal was to obtain their photometric redshifts ( $z_{\text{ph}}$ ), which were allowed to vary between  $z = 0$  to 25 in the fitting process. The settings for each tool are as follows.

- *Le Phare*: we constructed the templates using the population synthesis models of Bruzual & Charlot (2003, hereafter “BC03”) and the initial mass function (IMF) of Chabrier (2003). We adopted an exponentially declining star formation history (SFH), i.e.,  $\text{SFR} \propto e^{-t/\tau}$ , where  $\tau$  ranges from 0 to 13 Gyr. We applied the Calzetti’s extinction law (Calzetti et al. 1994; Calzetti 2001) with  $E(B-V)$  ranging from 0 to 1 mag at a step size of 0.1 mag. The option to include the contribution from emission lines was turned on.

- *EAZY*: we used the template set GALSEDATLAS of Brown et al. (2014), which was retrieved from MAST<sup>2</sup>. This set includes the spectra of 129 nearby galaxies of different types, which cover the UV-to-mid-IR wavelength range. Presumably, using this set of templates would optimize the fitting at low redshifts.

- *CIGALE*: we adopted a grid of CIGALE templates that include those using a delayed  $\tau$  model with  $0.01 < \tau \leq 13$  Gyr, a recent starburst, and the simple stellar population (SSP) models (i.e., single bursts) from BC03 assuming Chabrier IMF; we fixed the metallicity to  $Z = 0.02$ . We set the nebular emission contribution with

$-4 < \log U < -1$  and at a step size of 0.5. We also adopted a modified Calzetti’s extinction law under the `dust_modified_starburst` module with the color excess of nebular gas  $E(B-V)_g$  ranging from 0 to 3 mag at a step of 0.2 mag, and a fixed multiplication factor of 0.44 to apply on  $E(B-V)_g$  to calculate the stellar continuum attenuation  $E(B-V)_s$ . There are a lot of cases where the bright dropouts have enhanced emission in the central region increasing with wavelength, which could be caused by AGN. To investigate this probability, we included the `skirtor2016` AGN models from Stalevski et al. (2012, 2016). We varied the AGN fraction (hereafter  $f_{\text{AGN}}$ ), i.e., the AGN contribution to  $L_{\text{IR}}$ , from 0 to 1 at a step size of 0.2. We set the viewing angles at either  $30^\circ$  or  $70^\circ$  for Type 1 or 2 AGNs, respectively. We noticed that the program would run into errors when  $f_{\text{AGN}} = 1$ , and we resolved this by setting the maximum  $f_{\text{AGN}}$  to 0.999<sup>3</sup>. For the objects that do not show a compact central region at any passbands (in other words, their optical-to-IR emission is not likely due to AGN), we fixed their  $f_{\text{AGN}} = 0$ .

Examples of SED fitting results from these three runs are provided in Figure 3. We note on the treatment of the upper limits. For Le Phare, we set the magnitude error to  $-1$  when a given band has the upper limit imposed, and the routine rejected any fits that violated the upper limit. For EAZY, we used the modified code as described in Yan et al. (2023a,b) to achieve this functionality. For CIGALE, we set the fluxes to the upper limit and the corresponding flux errors to  $-1$  times the upper limit.

### 5.2. Categorizing Bright Dropouts

We divided the bright dropouts in the main sample into three categories based on their  $z_{\text{ph}}$ , namely, “High- $z$ ”, “Low- $z$ ” and “Undecided”. The “High- $z$ ” category consists of objects for which at least two SED fitting tools (among the three) consistently derive  $z_{\text{ph}} \geq 6.0$ . Similarly, the “Low- $z$ ” category consists of objects that have consistent  $z_{\text{ph}} < 6.0$  from at least two fitting tools. In both categories, we further ranked the objects into “Tier 1” (T1) and “Tier 2” (T2) depending on the goodness of fits and the consistency of the results. For practical purpose, we deemed the fits with raw  $\chi^2 \leq 100$  as “good” fits. For the “High- $z$ ” category, if an object has good fits and  $z_{\text{ph}} \geq 6.0$  from all three tools, it was put in T1; if it has good fits and  $z_{\text{ph}} \geq 6.0$  from only two tools, or if it has  $z_{\text{ph}} \geq 6.0$  from all three tools but the fits are not always good, it was placed in T2. The ranking for the “Low- $z$ ” category was done similarly, with a slightly more stringent requirement on the consistency of  $z_{\text{ph}}$ : if an object has good fits and consistent  $z_{\text{ph}}$  from all three tools so that the differences  $\Delta z_{\text{ph}} < 1.0$ , it was put in T1; if it has good fits and consistent  $z_{\text{ph}}$  from only two tools, or if it has consistent  $z_{\text{ph}}$  from all three tools but the fits are not always good, it was placed in T2. Finally, all objects that were not in

<sup>2</sup> <https://archive.stsci.edu/hlsp/galsedatlas>

<sup>3</sup> In the cases of CIGALE returning  $f_{\text{AGN}} = 0.999$ , they are reported as  $f_{\text{AGN}} = 1.0$ .



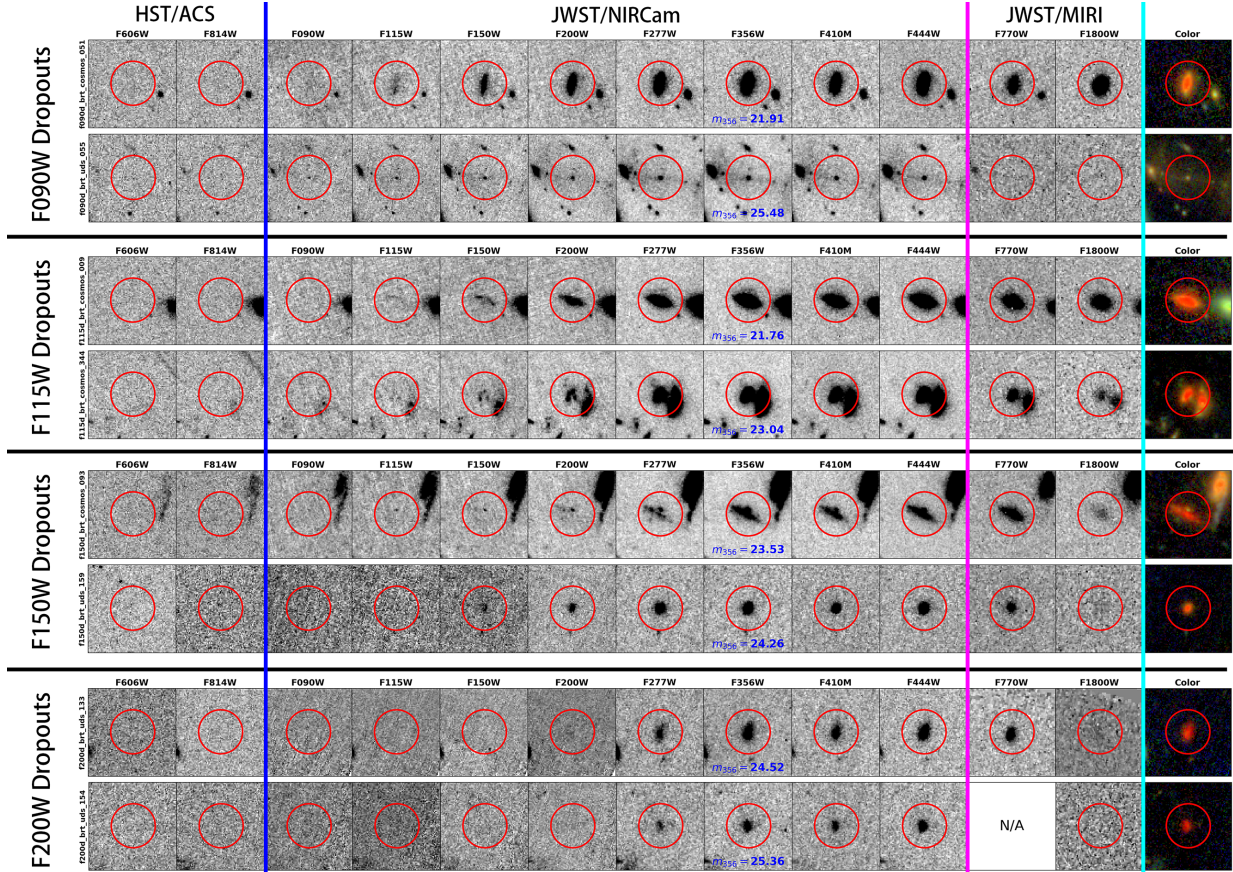


**Figure 1.** Image stamps of example very bright dropouts in F090W, F115W, F150W, and F200W, arranged from top to bottom. Two example objects are shown for each group. The stamps are  $2'' \times 2''$  in size and are oriented with north being up and east being left. The images are from the HST ACS, JWST NIRCcam and JWST MIRI, with the passbands as noted. Most of the very bright dropouts are either disk-like ( $\sim 40\%$ ) or compact ( $\sim 45\%$ ) in morphology in F356W, and one each is shown for the F090W, F150W and F200W dropouts. The example F115W dropouts include a disk-like object and an irregular object. Only  $\sim 15\%$  of the very bright dropouts have irregular morphology.

either the “High- $z$ ” or the “Low- $z$ ” category as ranked were assigned to the “Undecided” category.

- **High- $z$ :** We identified 10 high- $z$  candidates from the sample, among which 3 are in T1 and 7 are in T2. They are listed in Table 3 and 4, respectively, along with their physical properties derived from the SED analysis.

- **Low- $z$ :** There are 43 T1 and 50 T2 objects in this category, which are listed in Tables 5 and 6, respectively. Among the 93 objects, the vast majority of them have  $z_{\text{ph}} = 1-4$ .

- **Undecided:** This category contains 34 objects that cannot be placed in either category above. For the sake of completeness, they are listed in Table B.1.

In the  $m_{115} - m_{356}$  versus  $m_{356}$  distribution shown in Figure 2, the objects in the above three categories are indicated by different colors. It is obvious that many “High- $z$ ” objects can be classified as EROs under the fiducial criterion of  $m_{115} - m_{356} > 2.0$  mag. In total, 80%, 87% and 63% of the objects in the “High- $z$ ”, “Low- $z$ ” and “Undecided” categories can be classified as EROs, respectively.

Figure 4 shows the distribution of the fitted age and  $E(B - V)$  for the “Low- $z$ ” and “High- $z$ ” objects, which are the two most important (and degenerated) parameters that might give

low- $z$  galaxies red colors mimicking those of high- $z$  galaxies. As evident in the figure, the regions occupied by the two categories are not well separated. The contours of the “High- $z$ ” objects make a thin slab at the age of  $\sim 0.25$  Gyr, which is largely due to the constraint that the age of a galaxy cannot be older than that of the universe at the fitted high redshift. However, the region of the “Low- $z$ ” objects also extends to very close to this area.

Another interesting point revealed in our SED analysis is that incorporating mid-IR photometry, while being helpful, still does not provide a decisive factor to separate the low- $z$  and high- $z$  candidates. For example, contrary to one might naively believe, being bright in mid-IR does not necessarily preclude a good SED fit to give a high- $z$  solution (see Figure 3).

## 6. SPECTROSCOPIC IDENTIFICATIONS

As it turns out, ten of our bright dropouts in the main sample have existing NIRSPEC spectroscopic data, which we used to identify their redshifts. These data are from the following programs: PID 1213 (PI Luetzgendorf), 1215 (PI Luetzgendorf), 4233 (PIs de Graaff & Brammer), and 6585

Dropout Band	F090W	F115W	F150W	F200W	F277W	Total
<b>COSMOS</b>	29 (69)	10 (16)	15 (24)	1 (1)	0	55 (110)
High-z T1/T2	0/1	0/1	2/0	0/0	0	2/2
Low-z T1/T2	7/11	2/5	7/3	0/1	0	16/20
Undecided	10	2	3	0	0	15
<b>UDS</b>	21 (27)	20 (49)	17 (35)	4 (7)	0	62 (118)
High-z T1/T2	0/0	0/4	0/0	0/0	0	0/4
Low-z T1/T2	10/7	5/9	9/5	0/2	0	24/23
Undecided	4	2	3	2	0	11
<b>CEERS</b>	/	6 (37)	5 (13)	0 (2)	0	11 (52)
High-z T1/T2	/	0/1	1/0	0	0	1/1
Low-z T1/T2	/	2/2	0/2	0	0	2/4
Undecided	/	1	2	0	0	3
<b>GOODS-S</b>	9 (12)	0 (1)	0 (6)	0 (1)	0	9 (20)
High-z T1/T2	0/0	0/0	0	0	0	0/0
Low-z T1/T2	1/3	0/0	0	0	0	1/3
Undecided	5	0	0	0	0	5
<b>Total</b>	59 (108)	36 (103)	37 (78)	5 (11)	0	137 (300)

**Table 2.** Statistics of very bright dropouts in each field. For each field, the first row gives the total numbers of bright dropouts in the main sample (i.e., objects covered by at least one MIRI band), with the numbers in parentheses representing the total in the whole sample. The second and the third rows show the numbers of “High- $z$ ” and “Low- $z$ ” objects in T1 and T2 (separated by “/”), respectively. The fourth row is the number of “Undecided” objects. See Section 5.2 for details.

**Table 3.** Tier 1 “High- $z$ ” Objects

SID	R.A.	Decl.	$m_{356}$	$z_{lp}$	$z_{ez}$	$z_{cg}$	$\log(M_*) [M_\odot]$	$f_{AGN}$	$E(B-V)$	$\log(\text{SFR}) [M_\odot/\text{yr}]$	Morphology
f150d_brt.ceers_051	215.0313294	52.9171141	24.89	$12.22^{+0.24}_{-0.28}$	$14.57^{+0.01}_{-0.01}$	$14.38^{+0.62}_{-0.73}$	$11.47^{+0.06}_{-0.09}/11.90^{+0.37}_{-11.90}$	$\dots/0.62^{+0.27}_{-0.27}$	$0.7/0.82^{+0.41}_{-0.26}$	$5.36^{+0.40}_{-0.51}$	c
f150d_brt.cosmos_093	150.0651062	2.2636221	23.53	$10.66^{+0.25}_{-0.23}$	$11.06^{+0.02}_{-0.02}$	$9.95^{+0.13}_{-0.18}$	$10.86^{+0.20}_{-0.05}/10.99^{+0.07}_{-0.08}$	$\dots/0$	$0.5/0.59^{+0.05}_{-0.05}$	$3.91^{+0.29}_{-0.11}$	d
f150d_brt.cosmos_137	150.1089402	2.2936631	23.86	$8.81^{+0.27}_{-0.53}$	$11.68^{+0.22}_{-0.22}$	$10.75^{+2.31}_{-2.31}$	$11.11^{+0.04}_{-0.05}/11.17^{+0.29}_{-1.17}$	$\dots/0.35^{+0.24}_{-0.24}$	$0.7/0.60^{+0.21}_{-0.21}$	$4.07^{+0.09}_{-0.07}$	c

NOTE—The brightness of an object is indicated using  $m_{356}$ . The photometric redshifts from Le Phare, EAZY, and CIGALE are listed as  $z_{lp}$ ,  $z_{ez}$ , and  $z_{cg}$ , respectively. For Le Phare and EAZY, the photometric redshifts are the mean values weighted by the probability distribution function  $P(z)$ . For CIGALE,  $z_{cg}$  is the 50th percentile value and the errors indicate the 16th and 84th percentile values. The stellar mass ( $M_*$ ), reddening ( $E(B-V)$ ) and star formation rate (SFR) estimates are from the Le Phare and the CIGALE runs but are not available in the EAZY runs, and therefore only two sets of values are quoted (separated by “/”). The AGN fraction ( $f_{AGN}$ ) estimates are only available from CIGALE. The morphological classifications are given under the last column, where “c” stands for “compact” and “d” stands for “disk-like”.

**Table 4.** Tier 2 “High- $z$ ” Objects

SID	R.A.	Decl.	$m_{356}$	$z_{lp}$	$z_{ez}$	$z_{cg}$	$\log(M_*) [M_\odot]$	$f_{AGN}$	$E(B-V)$	$\log(\text{SFR}) [M_\odot/\text{yr}]$	Morphology
f115d_brt.ceers_062	215.0354323	52.8906847	24.92	$8.80^{+0.14}_{-0.14}$	$8.88^{+0.01}_{-0.01}$	$8.95^{+0.12}_{-0.12}$	$9.26^{+0.04}_{-0.04}/8.94^{+0.09}_{-0.11}$	$\dots/0.32^{+0.29}_{-0.29}$	$0.2/0.09^{+0.02}_{-0.02}$	$2.60^{+0.08}_{-0.07}/2.19^{+0.09}_{-0.09}$	c
f090d_brt.cosmos_663	150.0634749	2.3552383	23.56	$6.16^{+0.16}_{-0.16}$	$6.88^{+0.00}_{-0.00}$	$6.78^{+0.09}_{-0.09}$	$-9.04^{+0.09}_{-0.11}$	$-0.43^{+0.36}_{-0.36}$	$-0.01^{+0.03}_{-0.01}$	$-2.11^{+0.11}_{-0.11}$	c
f115d_brt.cosmos_270	150.0985778	2.3208768	22.75	$7.93^{+0.20}_{-0.83}$	$6.70^{+0.01}_{-0.01}$	$2.86^{+0.78}_{-0.78}$	$11.50^{+0.05}_{-0.09}$	$\dots/0$	$0.7/0.77^{+0.08}_{-0.08}$	$4.81^{+0.09}_{-0.18}$	d
f115d_brt.uds_089	34.2669263	-5.2947891	23.25	$8.37^{+0.23}_{-0.28}$	$2.64^{+0.07}_{-0.07}$	$7.62^{+1.15}_{-1.15}$	$10.76^{+0.04}_{-0.05}/10.69^{+0.26}_{-0.75}$	$\dots/0.44^{+0.29}_{-0.29}$	$0.5/0.52^{+0.23}_{-0.23}$	$3.69^{+0.08}_{-0.08}$	c
f115d_brt.uds_245	34.4716256	-5.256956	22.62	$8.78^{+0.15}_{-0.14}$	$2.46^{+0.02}_{-0.02}$	$8.55^{+1.47}_{-1.47}$	$10.99^{+0.04}_{-0.04}/10.49^{+0.41}_{-10.49}$	$\dots/0.72^{+0.23}_{-0.23}$	$0.5/0.48^{+0.34}_{-0.34}$	$4.04^{+0.08}_{-0.09}$	irr
f115d_brt.uds_647	34.2421684	-5.1472847	23.06	$8.66^{+0.17}_{-0.20}$	$2.54^{+0.02}_{-0.02}$	$7.54^{+2.24}_{-2.24}$	$10.80^{+0.04}_{-0.04}/10.74^{+0.15}_{-0.24}$	$\dots/0$	$0.5/0.54^{+0.06}_{-0.06}$	$3.79^{+0.07}_{-0.07}$	c
f115d_brt.uds_754	34.3546998	-5.1097457	22.57	$5.60^{+0.14}_{-0.14}$	$9.27^{+0.06}_{-0.02}$	$9.91^{+1.84}_{-1.84}$	$11.17^{+0.08}_{-0.05}/11.52^{+0.17}_{-0.27}$	$\dots/0$	$0.9/0.60^{+0.09}_{-0.09}$	$4.12^{+0.07}_{-0.09}$	irr

NOTE— Similar to Table 3 but for the Tier 2 objects in the “High- $z$ ” category. Some of the parameters derived by Le Phare are not available because of the very bad fits. The morphological type “irr” stands for “irregular”.

(PI Coultter). We used the data taken in the PRISM mode, which cover the range of 0.6-5.3  $\mu\text{m}$  with the resolving power of  $R \approx 30\text{--}300$ .

We reduced these data on our own. We first retrieved the Level 1b products from MAST and processed them through the `calwebb_detector1` step of the JWST pipeline (version 1.14.0) in the context of `jwst_1234.pmap`. The out-







**Table 7.** NIRSpec/MSA Identifications of Very Bright Dropouts

SID	Category (Tier)/Morph	$z_{\text{sp}}$	$z_{1p}$	$z_{\text{ez}}$	$z_{\text{cg}}$	T (Myr)	E(B-V)	$\log_{10}(M_*/M_{\odot})$
f115d_brt_uds_245	High- $z$ (T2)/irr	2.53 (I)	$8.78^{+0.15}_{-0.14}$	$2.46^{+0.02}_{-0.02}$	$8.55^{+1.47}_{-1.47}$	$-576 \pm 328$	$-0.44 \pm 0.07$	$-10.61 \pm 0.06$
f115d_brt_cosmos_344	Undecided/irr	2.99 (I)	$8.49^{+0.24}_{-0.49}$	$3.10^{+0.03}_{-0.03}$	$3.38^{+1.26}_{-1.26}$	$-1015 \pm 592$	$-0.56 \pm 0.10$	$-10.69 \pm 0.14$
f150d_brt_ceers_113	Undecided/c	3.10 (I)	$15.38^{+0.15}_{-0.14}$	$3.98^{+0.01}_{-0.01}$	$3.09^{+2.18}_{-2.18}$	$-934 \pm 288$	$-0.40 \pm 0.07$	$-10.40 \pm 0.05$
f115d_brt_ceers_279	Low- $z$ (T2)/c	3.21 (I)	$1.14^{+0.17}_{-0.14}$	$2.64^{+0.06}_{-0.06}$	$1.01^{+0.22}_{-0.22}$	$1575^{+217}_{-524}/1010 \pm 87$	$0.0/0.00 \pm 0.01$	$10.08^{+0.05}_{-0.25}/9.99 \pm 0.02$
f115d_brt_uds_685	Low- $z$ (T1)/c	3.23 (I)	$3.17^{+0.17}_{-0.16}$	$3.41^{+0.06}_{-0.06}$	$2.74^{+0.24}_{-0.24}$	$229^{+710}_{-206}/913 \pm 718$	$1.0/0.57 \pm 0.11$	$10.25^{+0.44}_{-0.25}/10.77 \pm 0.11$
f150d_brt_ceers_051	High- $z$ (T1)/c	3.46 (I)	$12.22^{+0.24}_{-0.28}$	$14.57^{+0.01}_{-0.01}$	$14.37^{+0.80}_{-0.80}$	$34^{+71}_{-19}/665 \pm 360$	$0.8/0.68 \pm 0.10$	$9.84^{+0.18}_{-0.22}/10.38 \pm 0.10$
f115d_brt_ceers_062	High- $z$ (T2)/c	8.679 (I)	$8.80^{+0.14}_{-0.14}$	$8.88^{+0.01}_{-0.01}$	$8.95^{+0.12}_{-0.12}$	$-13 \pm 8$	$-0.15 \pm 0.04$	$-9.10 \pm 0.08$
f150d_brt_uds_158	Low- $z$ (T2)/c	3.72 (II)	$3.39^{+7.41}_{-0.41}$	$3.44^{+0.16}_{-0.16}$	$2.45^{+0.90}_{-0.90}$	$82^{+454}_{-63}/1073 \pm 365$	$0.4/0.08 \pm 0.10$	$9.22^{+0.38}_{-0.25}/9.75 \pm 0.07$
f200d_brt_uds_154	Low- $z$ (T2)/c	4.56 (II)	$2.61^{+0.22}_{-0.20}$	$5.86^{+0.17}_{-0.17}$	$2.83^{+1.13}_{-1.13}$	$32^{+56}_{-18}/915 \pm 136$	$1.0/0.40 \pm 0.07$	$9.23^{+0.56}_{-0.37}/10.37 \pm 0.09$
f115d_brt_ceers_146	Low- $z$ (T1)/d	N/A (III)	$1.80^{+0.15}_{-0.15}$	$2.64^{+0.06}_{-0.06}$	$1.75^{+0.33}_{-0.33}$	-	-	-

NOTE—The Roman numerals in the parenthesis in the  $z_{\text{sp}}$  column indicate the reliability of the spectroscopic redshifts: I –  $z_{\text{sp}}$  determined using  $\geq 2$  high S/N emission lines; II – only one high S/N emission line is present, and  $z_{\text{sp}}$  is determined by assigning the most probable line considering its  $z_{\text{ph}}$ ; III – no emission line, i.e., no solid redshift can be determined.

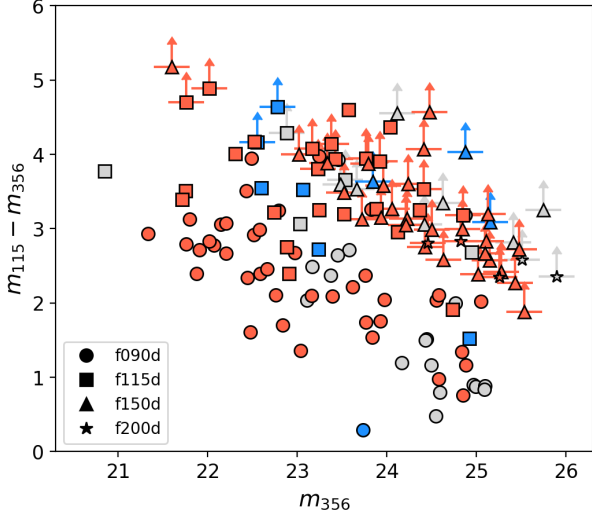


**Figure 2.** Observed  $m_{115} - m_{356}$  color versus  $m_{356}$  of the very bright dropouts in the main sample. The F090W, F115W, F150W, and F200W dropouts are represented by circles, squares, triangles, and stars, respectively. The ones with upward arrows indicate the lower limits of the color if the objects have  $S/N < 2.0$  in F115W, and the color lower limits are calculated using the  $2\sigma$  detection upper limits in this band. Adopting  $m_{115} - m_{356} > 2.0$  mag as the fiducial criterion for EROs, the vast majority (81%) of the very bright dropouts shown here would be selected. The objects in the “High- $z$ ”, “Low- $z$ ”, and “Undecided” categories (see Section 5.2 for details) are shown in blue, red, and gray, respectively.

fraction of real high- $z$  objects, which is also confirmed by the spectroscopic identifications. The caveat is that the SED screening for categorization is not ideal for these bright objects: our “High- $z$ ” category is severely contaminated, and there are still a large fraction of objects that have to be placed in the “Undecided” category. We believe that this is just a manifest of the limitation of SED fitting as a method in general: some low- $z$  galaxies can indeed have SEDs very similar to those of high- $z$  galaxies even when the photometry is extended to mid-IR, and it is very difficult for any fitting tools/templates to break the degeneracy.

## 7.2. Implication of bright dropouts at high- $z$

Bearing the aforementioned caveat in mind, we briefly discuss the implication of the possibility that some of these very bright dropouts could indeed be at high- $z$ . If they are at  $z > 6$  as their  $z_{\text{ph}}$  indicate, they must be the most extraordinary galaxies in the early universe. The recovered high- $z$  object, f115d\_brt\_ceers\_062 at  $z = 8.679$  (see also Tang et al. 2023; Larson et al. 2023; Isobe et al. 2023; Arrabal Haro et al. 2023, for the previous JWST identifications of the same object), is a good example. Interestingly, it has  $m_{115} - m_{356} = 1.52$  mag, which does not meet the ERO criterion that we adopt here but is very close. This galaxy was noted for its unusual brightness at such a high redshift and even more so for its very red color between the HST WFC3 F160W band ( $\sim 1.6 \mu\text{m}$ ) and the Spitzer IRAC Channel 2 ( $\sim 4.5 \mu\text{m}$ ), the latter of which was attributed to the strong [O III] emission lines being shifted to  $\sim 4.8 \mu\text{m}$  (Zitrin et al. 2015). The JWST spectrum confirms that it is indeed the case. This indicates that the galaxy has very active ongoing star formation, which is the reason that it is so luminous in the rest frame UV ( $M(1500\text{\AA}) = -22.4$  mag). As shown in Figure 5, the SED fitting by CIGALE at its  $z_{\text{sp}}$  gives the instantaneous SFR =  $232.9 \pm 80.5 M_{\odot} \text{ yr}^{-1}$ , which makes it qualified as a starburst. This extremely high SFR is the result of its high stellar mass ( $M_* = 10^{9.1} M_{\odot}$ ) and very young age ( $T = 12.7 \pm 7.8$  Myr), the latter of which is needed to explain its very blue UV emission. In fact, even with such an extreme solution, its  $m_{150} - m_{200}$  color is still not well explained; it is likely that an initial mass function more top-heavy than currently adopted will be necessary.

If more high- $z$  galaxies are identified in our sample, the most challenging issue will be explaining their stellar masses. Given their brightnesses in the two reddest NIRCcam bands (F356W and F444W), not only starburst-like SFRs but also very high stellar masses will be required to fit their SEDs reasonably. Some of our objects will have to have  $M_* \sim 10^{11} M_{\odot}$ , which, to our knowledge, cannot be produced in any simulations in the early universe. More extensive spectroscopic identifications will be needed to determine whether this poses a real problem.

## 8. SUMMARY

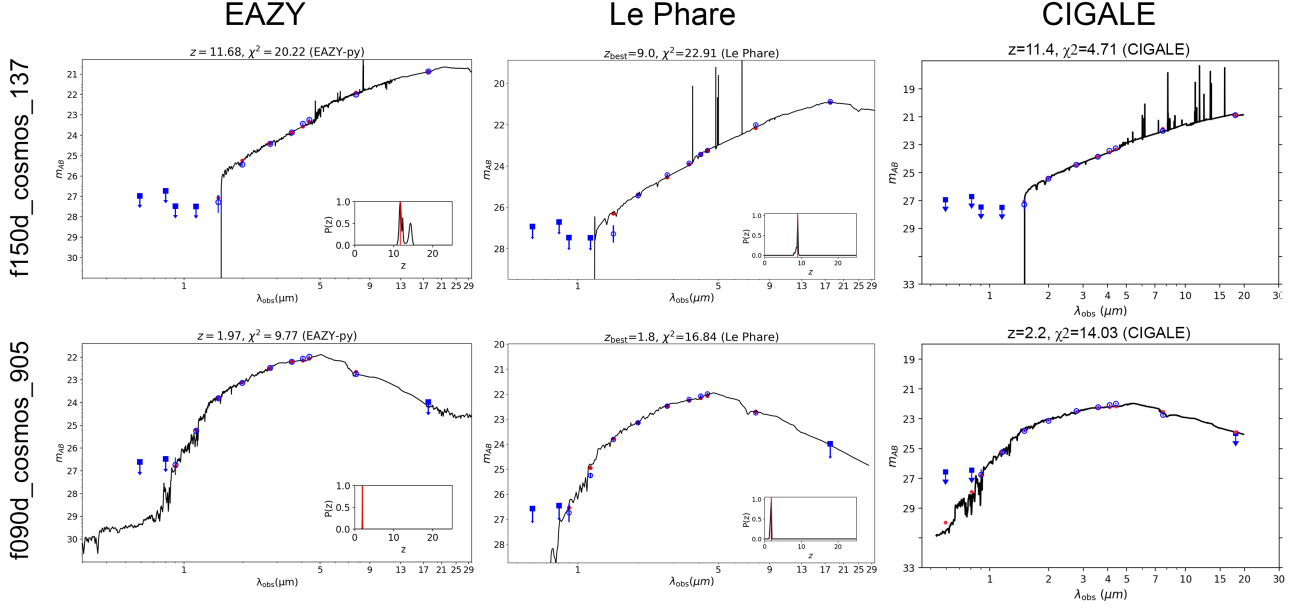


**Figure 3.** Examples of SED fitting results on one object in the “High- $z$  category (top panel) and one in the “Low- $z$ ” category (bottom panel). The blue symbols represent the observed values, and the curves are the spectra of the best-fit models. The red symbols are the synthesized magnitudes derived from the best-fit models. The insets show the probability distribution function of  $z_{\text{ph}}$ . The quoted  $z_{\text{ph}}$  value on top of each panel is from the shown best-fit model, which is slightly different from the adopted value (see Table 3 for further explanation.)

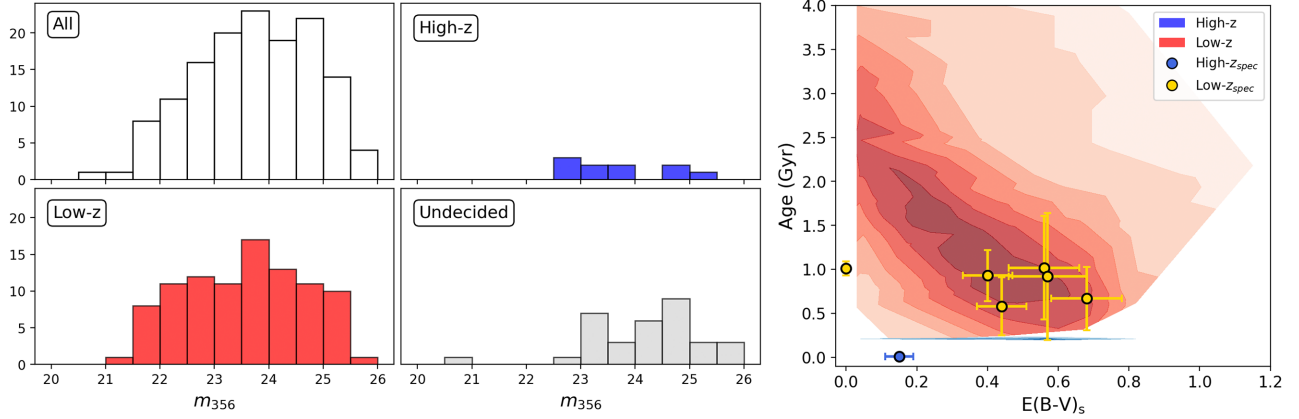


**Figure 4.** *Left:* F356W magnitude distributions for all objects, and objects in the “High- $z$ ”, “Low- $z$ ”, and “Undecided” categories, respectively. *Right:* Contour plots of Age vs.  $E(B-V)_s$  for the objects in the “High- $z$ ” (blue) and “Low- $z$ ” (red) categories. Both parameters are the 50th percentile values from the CIGALE run (using those from the Le Phare run gives similar results). The overlaid data points represent the SED fitting results of the seven spectroscopically confirmed grade I objects in Table 7 (see Section 6) when fixing the redshifts to their  $z_{\text{sp}}$ ; the only confirmed high- $z$  object is shown in blue, while all other objects (all at low redshifts) are shown in gold.

We present a systematic study of very bright dropouts in the successive JWST NIRCcam passbands, which was carried out using the public data in four blank fields over  $500 \text{ arcmin}^2$ . These objects were selected following the classic dropout method that is widely used to search for Lyman-break galaxies at high redshifts, with the only additional requirement that they must be very bright: the F090W and F115W dropouts must have  $m_{356} \leq 25.1 \text{ mag}$ , and the F150W and F200W dropouts must have  $m_{356} \leq 26.0 \text{ mag}$ . In total, there are 300 very bright dropouts selected. We then

focused on the 137 objects that fall within the coverage of the MIRI observations ( $\sim 200 \text{ arcmin}^2$  of overlapping area), which form the main sample of this work. The rationale was that the inclusion of the mid-IR measurements would constrain the SEDs more stringently. Using the fiducial criterion of  $m_{115} - m_{356} > 2.0 \text{ mag}$  for the ERO selection, the vast majority of them (81%) would qualify as EROs, although the usual ERO selection does not impose the criterion of non-detections in the veto bands as the dropout selection does. The goal of this study is to understand the nature of such very



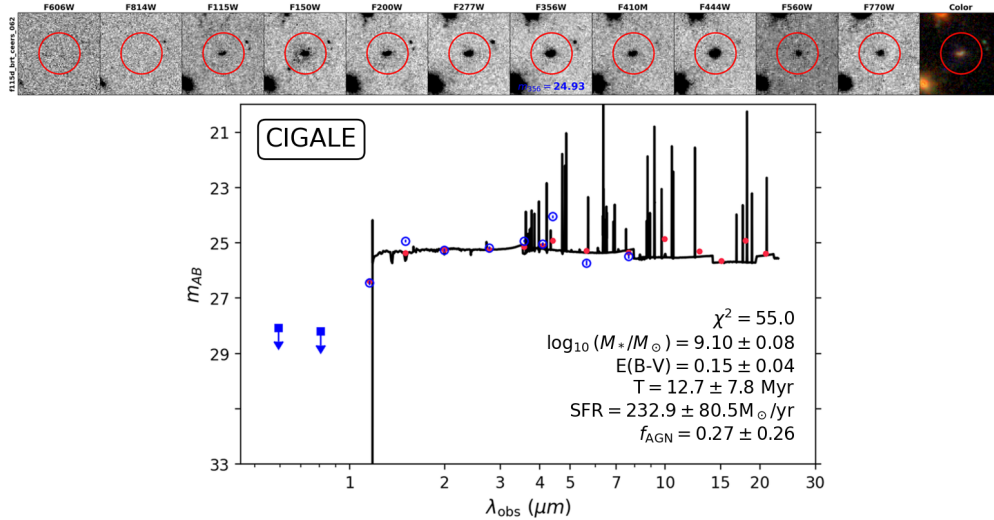


**Figure 5.** Image stamps of f115d\_brt\_ceers\_062 (top) and its SED fitting results from CIGALE (bottom). This is a known galaxy at  $z_{\text{sp}} = 8.679$  recovered in our selection. The image stamps are similar to those shown in Figure 1. The SED fitting plot is similar to those shown in Figure 3, but is obtained by running CIGALE at the fixed  $z = 8.679$ . The most important output physical parameters are shown.

bright dropouts, in particular how they overlap with the ERO population at low redshifts and whether any of them could be high- $z$  LBGs as the dropout method means to select.

For this purpose, we used three different fitting tools to analyze their SEDs independently, each using a different set of fitting templates: Le Phare with the BC03 population synthesis models, EAZY with the spectra of 129 nearby galaxies from Brown et al. (2014) that have mid-IR measurements, and CIGALE with the BC03 models for stars plus the contributions from the nebular gas and the possible AGN component. Based on the derived  $z_{\text{ph}}$  values, we divided our objects into two categories, the “High- $z$ ” category containing objects with  $z_{\text{ph}} \geq 6.0$  and the “Low- $z$ ” category containing those with  $z_{\text{ph}} < 6.0$ . In each category, we further sorted the objects into Tier 1 and Tier 2 based on the goodness of fits and the internal consistency from three SED fitting tools. Any objects that could not be classified as “High- $z$ ” or “Low- $z$ ” were put in the “Undecided” category. In the end, there are 10 objects in “High- $z$ ” (80% qualify as EROs), 93 in “Low- $z$ ” (87% EROs) and 34 in “Undecided” (63% EROs). Therefore,

our main conclusions are that (1) the NIRCcam-selected very-bright dropouts are predominantly ( $> 67.9\%$ ) low- $z$  galaxies and (2) a non-negligible fraction ( $> 7\%$ ) of them could still be at high- $z$ .

Ten of our objects have existing JWST NIRSspec spectroscopic observations, and we have obtained secure redshifts for seven of them. Among these seven objects, six are at  $z \approx 3$  (including two objects in our “High- $z$ ” category), and one is the recovery of a known galaxy at  $z = 8.679$  that is a Tier 2 object in our “High- $z$ ” category. These identifications, while still very limited, are consistent with our conclusions above. Although the “High- $z$ ” category is severely contaminated at such a bright level despite the inclusion of the mid-IR data, it does contain at least one genuine high- $z$  object. If more high- $z$  objects are confirmed, they could pose severe challenge to theories to explain their extremely high SFR and stellar masses.

The authors acknowledge the support from the University of Missouri Research Council grant URC-23-029 and the NSF grant AST-2307447.

## REFERENCES

- Alcalde Pampliega, B., Pérez-González, P. G., Barro, G., et al. 2019, *ApJ*, 876, 135, doi: [10.3847/1538-4357/ab14f2](https://doi.org/10.3847/1538-4357/ab14f2)
- Arnouts, S., Cristiani, S., Moscardini, L., et al. 1999, *MNRAS*, 310, 540, doi: [10.1046/j.1365-8711.1999.02978.x](https://doi.org/10.1046/j.1365-8711.1999.02978.x)
- Arrabal Haro, P., Dickinson, M., Finkelstein, S. L., et al. 2023, *ApJL*, 951, L22, doi: [10.3847/2041-8213/acdd54](https://doi.org/10.3847/2041-8213/acdd54)
- Barrufet, L., Oesch, P. A., Weibel, A., et al. 2023, *MNRAS*, 522, 449, doi: [10.1093/mnras/stad947](https://doi.org/10.1093/mnras/stad947)
- Bertin, E., & Arnouts, S. 1996, *A&AS*, 117, 393, doi: [10.1051/aas:1996164](https://doi.org/10.1051/aas:1996164)
- Boquien, M., Burgarella, D., Roehlly, Y., et al. 2019, *A&A*, 622, A103, doi: [10.1051/0004-6361/201834156](https://doi.org/10.1051/0004-6361/201834156)
- Brammer, G. 2023, msaexp: NIRSspec analysis tools, 0.6.17, Zenodo, doi: [10.5281/zenodo.7299500](https://doi.org/10.5281/zenodo.7299500)
- Brammer, G. B., van Dokkum, P. G., & Coppi, P. 2008, *ApJ*, 686, 1503, doi: [10.1086/591786](https://doi.org/10.1086/591786)

- Brown, M. J. I., Moustakas, J., Smith, J. D. T., et al. 2014, *ApJS*, 212, 18, doi: [10.1088/0067-0049/212/2/18](https://doi.org/10.1088/0067-0049/212/2/18)
- Bruzual, G., & Charlot, S. 2003, *MNRAS*, 344, 1000, doi: [10.1046/j.1365-8711.2003.06897.x](https://doi.org/10.1046/j.1365-8711.2003.06897.x)
- Bushouse, H., Eisenhamer, J., Dencheva, N., et al. 2024, JWST Calibration Pipeline, 1.14.0, Zenodo, doi: [10.5281/zenodo.6984365](https://doi.org/10.5281/zenodo.6984365)
- Calzetti, D. 2001, *PASP*, 113, 1449, doi: [10.1086/324269](https://doi.org/10.1086/324269)
- Calzetti, D., Kinney, A. L., & Storchi-Bergmann, T. 1994, *ApJ*, 429, 582, doi: [10.1086/174346](https://doi.org/10.1086/174346)
- Caputi, K. I., Michałowski, M. J., Krips, M., et al. 2014, *ApJ*, 788, 126, doi: [10.1088/0004-637X/788/2/126](https://doi.org/10.1088/0004-637X/788/2/126)
- Carniani, S., Hainline, K., D'Eugenio, F., et al. 2024, *Nature*, 633, 318, doi: [10.1038/s41586-024-07860-9](https://doi.org/10.1038/s41586-024-07860-9)
- Chabrier, G. 2003, *PASP*, 115, 763, doi: [10.1086/376392](https://doi.org/10.1086/376392)
- Cowie, L. L., Barger, A. J., Wang, W. H., & Williams, J. P. 2009, *ApJL*, 697, L122, doi: [10.1088/0004-637X/697/2/L122](https://doi.org/10.1088/0004-637X/697/2/L122)
- Dunlop, J. S., Abraham, R. G., Ashby, M. L. N., et al. 2021, PRIMER: Public Release IMaging for Extragalactic Research, JWST Proposal. Cycle 1, ID. #1837
- Eisenstein, D. J., Willott, C., Alberts, S., et al. 2023a, arXiv e-prints, arXiv:2306.02465, doi: [10.48550/arXiv.2306.02465](https://doi.org/10.48550/arXiv.2306.02465)
- Eisenstein, D. J., Maiolino, R., Alberts, S., et al. 2023b, Unveiling the Redshift Frontier with JWST, JWST Proposal. Cycle 2, ID. #3215
- Elston, R., Rieke, G. H., & Rieke, M. J. 1988, *ApJL*, 331, L77, doi: [10.1086/185239](https://doi.org/10.1086/185239)
- Ferreira, L., Adams, N., Conselice, C. J., et al. 2022, *ApJL*, 938, L2, doi: [10.3847/2041-8213/ac947c](https://doi.org/10.3847/2041-8213/ac947c)
- Ferreira, L., Conselice, C. J., Sazonova, E., et al. 2023, *ApJ*, 955, 94, doi: [10.3847/1538-4357/acec76](https://doi.org/10.3847/1538-4357/acec76)
- Finkelstein, S. L., Bagley, M. B., Ferguson, H. C., et al. 2023, *ApJL*, 946, L13, doi: [10.3847/2041-8213/acade4](https://doi.org/10.3847/2041-8213/acade4)
- Fudamoto, Y., Inoue, A. K., & Sugahara, Y. 2022, *ApJL*, 938, L24, doi: [10.3847/2041-8213/ac982b10.48550/arXiv.2208.00132](https://doi.org/10.3847/2041-8213/ac982b10.48550/arXiv.2208.00132)
- Gibson, J. L., Nelson, E., Williams, C. C., et al. 2024, *ApJ*, 974, 48, doi: [10.3847/1538-4357/ad64c2](https://doi.org/10.3847/1538-4357/ad64c2)
- Gómez-Guijarro, C., Elbaz, D., Xiao, M., et al. 2022, *A&A*, 658, A43, doi: [10.1051/0004-6361/202141615](https://doi.org/10.1051/0004-6361/202141615)
- Gómez-Guijarro, C., Magnelli, B., Elbaz, D., et al. 2023, *A&A*, 677, A34, doi: [10.1051/0004-6361/202346673](https://doi.org/10.1051/0004-6361/202346673)
- Grogin, N. A., Kocevski, D. D., Faber, S. M., et al. 2011, *ApJS*, 197, 35, doi: [10.1088/0067-0049/197/2/35](https://doi.org/10.1088/0067-0049/197/2/35)
- Hu, E. M., & Ridgway, S. E. 1994, *AJ*, 107, 1303, doi: [10.1086/116943](https://doi.org/10.1086/116943)
- Ilbert, O., Arnouts, S., McCracken, H. J., et al. 2006, *A&A*, 457, 841, doi: [10.1051/0004-6361:20065138](https://doi.org/10.1051/0004-6361:20065138)
- Isobe, Y., Ouchi, M., Tominaga, N., et al. 2023, *ApJ*, 959, 100, doi: [10.3847/1538-4357/ad09be](https://doi.org/10.3847/1538-4357/ad09be)
- Jacobs, C., Glazebrook, K., Calabrò, A., et al. 2023, *ApJL*, 948, L13, doi: [10.3847/2041-8213/accd6d](https://doi.org/10.3847/2041-8213/accd6d)
- Koekemoer, A. M., Faber, S. M., Ferguson, H. C., et al. 2011, *ApJS*, 197, 36, doi: [10.1088/0067-0049/197/2/36](https://doi.org/10.1088/0067-0049/197/2/36)
- Kuhn, V., Guo, Y., Martin, A., et al. 2024, *ApJL*, 968, L15, doi: [10.3847/2041-8213/ad43eb](https://doi.org/10.3847/2041-8213/ad43eb)
- Larson, R. L., Finkelstein, S. L., Kocevski, D. D., et al. 2023, *ApJL*, 953, L29, doi: [10.3847/2041-8213/ace619](https://doi.org/10.3847/2041-8213/ace619)
- Ling, C., & Yan, H. 2022, *ApJ*, 929, 40, doi: [10.3847/1538-4357/ac57c1](https://doi.org/10.3847/1538-4357/ac57c1)
- Nelson, E. J., Suess, K. A., Bezanson, R., et al. 2023, *ApJL*, 948, L18, doi: [10.3847/2041-8213/acc1e1](https://doi.org/10.3847/2041-8213/acc1e1)
- Norgaard-Nielsen, H. U., & Perez-Gonzalez, P. G. 2017, The MIRI HUDF Deep Imaging Survey, JWST Proposal. Cycle 1, ID. #1283
- Rieke, G., Alberts, S., Lyu, J., Morrison, J., & Shivaei, I. 2017, MIRI in the Hubble Ultra-Deep Field, JWST Proposal. Cycle 1, ID. #1207
- Robertson, B. E., Tacchella, S., Johnson, B. D., et al. 2023, *ApJL*, 942, L42, doi: [10.3847/2041-8213/aca08610.48550/arXiv.2208.11456](https://doi.org/10.3847/2041-8213/aca08610.48550/arXiv.2208.11456)
- Rodighiero, G., Bisigello, L., Iani, E., et al. 2023, *MNRAS*, 518, L19, doi: [10.1093/mnras/518l115](https://doi.org/10.1093/mnras/518l115)
- Scodreggio, M., & Silva, D. R. 2000, *A&A*, 359, 953, doi: [10.48550/arXiv.astro-ph/0004228](https://doi.org/10.48550/arXiv.astro-ph/0004228)
- Stalevski, M., Fritz, J., Baes, M., Nakos, T., & Popović, L. Č. 2012, *MNRAS*, 420, 2756, doi: [10.1111/j.1365-2966.2011.19775.x](https://doi.org/10.1111/j.1365-2966.2011.19775.x)
- Stalevski, M., Ricci, C., Ueda, Y., et al. 2016, *MNRAS*, 458, 2288, doi: [10.1093/mnras/stw444](https://doi.org/10.1093/mnras/stw444)
- Steidel, C. C., & Hamilton, D. 1992, *AJ*, 104, 941, doi: [10.1086/116287](https://doi.org/10.1086/116287)
- . 1993, *AJ*, 105, 2017, doi: [10.1086/116579](https://doi.org/10.1086/116579)
- Steidel, C. C., Pettini, M., & Hamilton, D. 1995, *AJ*, 110, 2519, doi: [10.1086/117709](https://doi.org/10.1086/117709)
- Tang, M., Stark, D. P., Chen, Z., et al. 2023, *MNRAS*, 526, 1657, doi: [10.1093/mnras/stad2763](https://doi.org/10.1093/mnras/stad2763)
- Thompson, D., Beckwith, S. V. W., Fockenbrock, R., et al. 1999, *ApJ*, 523, 100, doi: [10.1086/307708](https://doi.org/10.1086/307708)
- Walter, F., Decarli, R., Carilli, C., et al. 2012, *Nature*, 486, 233, doi: [10.1038/nature11073](https://doi.org/10.1038/nature11073)
- Wang, T., Elbaz, D., Schreiber, C., et al. 2016, *ApJ*, 816, 84, doi: [10.3847/0004-637X/816/2/84](https://doi.org/10.3847/0004-637X/816/2/84)
- Wang, T., Schreiber, C., Elbaz, D., et al. 2019, *Nature*, 572, 211, doi: [10.1038/s41586-019-1452-4](https://doi.org/10.1038/s41586-019-1452-4)
- Wang, W.-H., Barger, A. J., & Cowie, L. L. 2012, *ApJ*, 744, 155, doi: [10.1088/0004-637X/744/2/155](https://doi.org/10.1088/0004-637X/744/2/155)
- Williams, C. C., Oesch, P. A., Weibel, A., et al. 2024, arXiv e-prints, arXiv:2410.01875, doi: [10.48550/arXiv.2410.01875](https://doi.org/10.48550/arXiv.2410.01875)
- Xiao, M. Y., Elbaz, D., Gómez-Guijarro, C., et al. 2023, *A&A*, 672, A18, doi: [10.1051/0004-6361/202245100](https://doi.org/10.1051/0004-6361/202245100)

- Yan, H., Ma, Z., Ling, C., Cheng, C., & Huang, J.-S. 2023a, ApJL, 942, L9, doi: [10.3847/2041-8213/aca80c](https://doi.org/10.3847/2041-8213/aca80c)
- Yan, H., Sun, B., & Ling, C. 2024, ApJ, 975, 44, doi: [10.3847/1538-4357/ad7de9](https://doi.org/10.3847/1538-4357/ad7de9)
- Yan, H., Sun, B., Ma, Z., & Ling, C. 2023b, arXiv e-prints, arXiv:2311.15121, doi: [10.48550/arXiv.2311.15121](https://doi.org/10.48550/arXiv.2311.15121)
- Yan, H., Dickinson, M., Eisenhardt, P. R. M., et al. 2004, ApJ, 616, 63, doi: [10.1086/424898](https://doi.org/10.1086/424898)
- Yan, L., McCarthy, P. J., Weymann, R. J., et al. 2000, AJ, 120, 575, doi: [10.1086/301454](https://doi.org/10.1086/301454)
- Yang, G., Papovich, C., Bagley, M. B., et al. 2023, ApJL, 956, L12, doi: [10.3847/2041-8213/acfaa0](https://doi.org/10.3847/2041-8213/acfaa0)
- Zhou, L., Elbaz, D., Franco, M., et al. 2020, A&A, 642, A155, doi: [10.1051/0004-6361/202038059](https://doi.org/10.1051/0004-6361/202038059)
- Zitrin, A., Labbé, I., Belli, S., et al. 2015, ApJL, 810, L12, doi: [10.1088/2041-8205/810/1/L12](https://doi.org/10.1088/2041-8205/810/1/L12)



## APPENDIX

## A. THE SUPPLEMENT SAMPLE OF VERY BRIGHT DROPOUTS

Among the 300 very bright dropouts, 163 of them are outside of the MIRI coverage, which we did not perform SED analysis due to the lack of the mid-IR data. These objects form our supplement sample, which are listed below.







B. VERY BRIGHT DROPOUTS IN THE  
“UNDECIDED” CATEGORY IN THE MAIN  
SAMPLE

The objects in the main sample that cannot be placed in either the “High- $z$ ” or the “Low- $z$ ” categories were assigned as “Undecided”, which are given in the table below.

SID	R.A.	Decl.	$m_{356}$	SID	R.A.	Decl.	$m_{356}$
f115d_brt.ceers_430	214.751589	52.8299477	24.90	f150d_brt.ceers_113	214.8296653	52.8207925	24.11
f150d_brt.ceers_163	214.7678858	52.8163009	25.70	f090d_brt.cosmos_244	150.0775622	2.264394	25.13
f090d_brt.cosmos_351	150.0850761	2.2854155	23.15	f090d_brt.cosmos_363	150.0708811	2.2893357	23.40
f090d_brt.cosmos_395	150.0994053	2.2972383	23.20	f090d_brt.cosmos_419	150.098576	2.3012176	23.10
f090d_brt.cosmos_498	150.1762613	2.3194308	24.27	f090d_brt.cosmos_790	150.1835939	2.3903725	25.12
f090d_brt.cosmos_796	150.1557834	2.392438	24.52	f090d_brt.cosmos_919	150.1642394	2.4531855	23.51
f090d_brt.cosmos_927	150.1848911	2.4604111	25.25	f115d_brt.cosmos_010	150.0971618	2.1745523	23.54
f115d_brt.cosmos_344	150.14326	2.3560209	23.04	f150d_brt.cosmos_231	150.1819653	2.3355567	23.68
f150d_brt.cosmos_368	150.13919	2.4319799	21.61	f150d_brt.cosmos_394	150.1472663	2.4740686	24.45
f090d_brt.jsdeep_283	53.2063219	-27.7757229	24.68	f090d_brt.jsmed_040	53.0811514	-27.902613	25.09
f090d_brt.jsmed_126	53.0528574	-27.8777309	23.45	f090d_brt.jsmed_174	53.0796299	-27.870759	24.88
f090d_brt.jsmed_186	53.1015139	-27.8699644	23.45	f090d_brt.uds_076	34.4887416	-5.2656961	25.09
f090d_brt.uds_225	34.3544488	-5.1593633	24.70	f090d_brt.uds_254	34.4897227	-5.1457693	25.09
f090d_brt.uds_260	34.3822548	-5.1435204	24.43	f115d_brt.uds_640	34.3650612	-5.1488379	22.92
f115d_brt.uds_749	34.3749038	-5.1129002	20.86	f150d_brt.uds_057	34.4969958	-5.2899889	25.46
f150d_brt.uds_097	34.3248951	-5.2712995	24.66	f150d_brt.uds_361	34.2744535	-5.1437765	23.47
f200d_brt.uds_044	34.3411055	-5.2964632	25.89	f200d_brt.uds_420	34.4054154	-5.1393098	25.55

**Table B.1.** Objects in the “Undecided” category.